

Transport Dynamics of Water Molecules Confined between Lipid Membranes

Minho Lee^{1, 2}, Euihyun Lee³, Ji-hyun Kim^{1, 2}, Hyonseok Hwang⁶, Minhaeng Cho^{4, 5}, and
Jaeyoung Sung^{1, 2*}*

¹ Creative Research Initiative Center for Chemical Dynamics in Living Cells, Chung-Ang University, Seoul 06974, Republic of Korea

² Department of Chemistry, Chung-Ang University, Seoul 06974, Republic of Korea

³ Department of Chemistry, The University of Texas at Austin, TX 78757, USA

⁴ Center for Molecular Spectroscopy and Dynamics, Institute for Basic Science (IBS), Seoul 02841, Republic of Korea

⁵ Department of Chemistry, Korea University, Seoul 02841, Republic of Korea

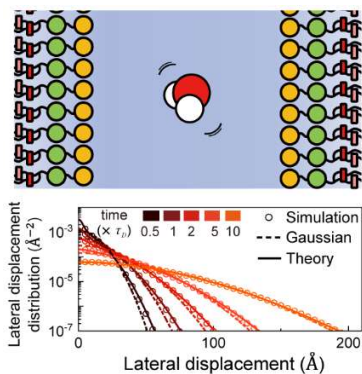
⁶ Department of Chemistry, Institute for Molecular Science and Fusion Technology, Kangwon National University, Chuncheon, Gangwon-do 24341, Republic of Korea

*Correspondence and requests for materials should be addressed to J.S. (email: jaeyoung@cau.ac.kr) and M.C. (email: mcho@korea.ac.kr).

ABSTRACT

Water molecules confined between biological membranes exhibit a distinctive non-Gaussian displacement distribution, far different from bulk water. Here, we introduce a new transport equation for water molecules in the intermembrane space, quantitatively explaining molecular dynamics simulation results. We find the unique transport dynamics of water molecules stems from the lateral diffusion coefficient fluctuation caused by their longitudinal motion. We also identify an interfacial region where water possesses distinct physical properties, unaffected by changes in the intermembrane separation.

TOC GRAPHICS



KEYWORDS

Nanochannel, Lipid bilayers, Heterogeneity, Complex fluids, Transport equation

Water confined in biological nanospaces, such as the inter-membrane regions of mitochondria, synaptic clefts, and endoplasmic reticula, is a crucial element for cell function¹⁻³. Extensive research has investigated the structure and dynamics of water molecules in the vicinity of phosphatidylcholine (PC) bilayers, a major component of biological membranes. These works employed various methods including IR pump-probe spectroscopy⁴⁻⁶, heterodyne-detected vibration sum frequency generation (HD-VSFG)^{7,8}, nuclear magnetic resonance (NMR)⁹, microfluidics¹⁰⁻¹², and molecular dynamics (MD) simulation¹³⁻²¹. It is now established that the motility of nanoconfined water increases with its distance from the membrane center, with which the major functional groups of PC phospholipids interacting with water molecules change^{4,9,14,17,18}. Moreover, it has been observed that dynamic motility fluctuations lead to Fickian-yet-non-Gaussian diffusion in complex fluids²². Despite these studies, however, a quantitative understanding of the time-dependent displacement distribution of nanoconfined water molecules has not yet been achieved.

To address this issue, we introduce a transport equation describing the thermal motion of molecules confined between two planar surfaces. Using MD simulations, we investigate the time-dependent displacement distribution of water molecules nanoconfined between two lipid membranes composed of 1,2-dimyristoyl-sn-glycero-3-phosphocholine (DMPC) lipids. The solution derived from our transport equation provides a quantitative explanation of the MD simulation results for the mean square displacement, the non-Gaussian parameter, and the displacement distribution. Our analysis shows that nanoconfined water exhibits a super-Gaussian lateral displacement distribution originating from dynamic fluctuations of the lateral diffusion coefficient due to its coupling to water motion in the longitudinal direction. The time-dependent deviation of this lateral displacement distribution from Gaussian is found to be strongly influenced

by the intermembrane separation. We also identify an interfacial region where water molecules have structure and dynamics that are distinct from bulk water and robust with respect to changes in intermembrane separation.

The essential assumption underlying our transport equation is that the most important variable that affects the lateral thermal motion of an interfacial water molecule is the distance, z , between the water molecule and the center of the membrane. This is a legitimate assumption because the microscopic environment interacting with a water molecule, including the functional groups of lipid molecules and hydrogen bond network, drastically changes with z ^{9,17,18}. Under this assumption, we obtain the following transport equation governing transport dynamics of interfacial water, starting from a general model of thermal motion coupled to environmental variables²³:

$$\hat{p}(\mathbf{r}_{\parallel}, z, s) = \hat{D}_{\parallel}(z, s) \nabla_{\parallel}^2 \hat{p}(\mathbf{r}_{\parallel}, z, s) + L(z) \hat{p}(\mathbf{r}_{\parallel}, z, s), \quad (1)$$

where $\hat{p}(\mathbf{r}_{\parallel}, z, s)$ denotes the Laplace transform of the joint probability density, $p(\mathbf{r}_{\parallel}, z, t)$, that a water molecule is located at lateral position \mathbf{r}_{\parallel} ($= (x, y)$) and the distance between the water molecule and the center of the membrane is z at time t . $\hat{f}(s)$ and $\hat{\partial}_i f(s)$ denote the Laplace transform of $f(t)$ and $\partial_i f(t)$, i.e., $\hat{f}(s) = \int_0^{\infty} dt e^{-st} f(t)$ and $\hat{\partial}_i f(s) = \int_0^{\infty} dt e^{-st} \partial_i f(t)$. ∇_{\parallel}^2 denotes the Laplacian in the two-dimensional space parallel to the lipid membrane. In eq 1, $\hat{D}_{\parallel}(z, s)$ represents the lateral diffusion kernel dependent on z . Its small- s limit, $\hat{D}_{\parallel}(z, 0)$, serves as the lateral diffusion coefficient, $D_{\parallel}(z)$, of water molecules separated by z from the center of the membrane. In eq 1, $L(z)$ denotes a mathematical operator describing the transport dynamics of the water molecules in a perpendicular direction to the membrane surface.

We then investigate the mean square displacement (MSD), $\Delta_2(t)$, and non-Gaussian parameters (NGP), $\alpha_2(t) \left[\equiv \Delta_4(t)/(2\Delta_2(t)^2) - 1 \right]$, of the lateral displacement distribution of the water molecules. Here, $\Delta_2(t)$ and $\Delta_4(t)$ denote the second and fourth moments of the time-dependent distribution of the water displacement, $\Delta \mathbf{r}_{\parallel}(t) \left[\equiv \mathbf{r}_{\parallel}(t) - \mathbf{r}_{\parallel}(0) \right]$, in the lateral direction. The NGP vanishes when the displacement distribution is Gaussian^{24,25}. From eq 1, analytic expressions of the $\Delta_2(t)$ and $\Delta_4(t)$ can be obtained as

$$\hat{\Delta}_2(s) = \frac{4}{s^2} \langle \hat{\mathcal{D}}_{\parallel}(s) \rangle, \quad (2a)$$

$$\hat{\Delta}_4(s) = 4s\hat{\Delta}_2(s)^2 \left[1 + s\hat{C}_{\mathcal{D}}(s) \right]. \quad (2b)$$

In eq 2a, $\langle \mathcal{D}_{\parallel}(t) \rangle$ denotes the mean diffusion kernel of water molecules. $\langle Q \rangle$ designates the average of quantity $Q(z)$ over the equilibrium distribution, $P_{eq}(z)$, of z . $\langle \mathcal{D}_{\parallel}(t) \rangle$ is the same as the lateral velocity autocorrelation function (VAF) of water molecules divided by 2^{23} . In eq 2b, $C_{\mathcal{D}}(t)$ denotes the lateral diffusion kernel correlation (DKC) defined by

$$\hat{C}_{\mathcal{D}}(s) = \int_0^{\ell} dz \int_0^{\ell} dz_0 \frac{\delta \hat{\mathcal{D}}_{\parallel}(z, s)}{\langle \hat{\mathcal{D}}_{\parallel}(s) \rangle} \hat{G}(z, s | z_0) \frac{\delta \hat{\mathcal{D}}_{\parallel}(z_0, s)}{\langle \hat{\mathcal{D}}_{\parallel}(s) \rangle} P_{eq}(z_0), \quad (3)$$

where 0 and ℓ denote the center positions of the two membranes confining water molecules (see Figure 1). In eq 3, $\delta \hat{\mathcal{D}}_{\parallel}(z, s)$ and $G(z, t | z_0)$ denote, respectively, $\hat{\mathcal{D}}_{\parallel}(z, s) - \langle \hat{\mathcal{D}}_{\parallel}(s) \rangle$ and the Green's function, or the conditional probability that a water molecule initially located at z_0 is found at z at time t , defined by $\partial_t G(z, t | z_0) = L(z)G(z, t | z_0)$ with the initial condition, $G(z, 0 | z_0) = \delta(z - z_0)$. Equation 2 enables us to extract the time profile of the DKC from the

MSD and the NGP or the first two nonvanishing moments of the displacement distribution (see Figure S3a in Supporting Information).

At the onset of Fickian diffusion, the NGP reaches its maximum value (Figure 2). Beyond this NGP peak time, the MSD of water molecules linearly increases with time, which results because the VAF or $\langle \mathcal{D}_{\parallel}(t) \rangle$ is negligibly small after the NGP peak time, i.e.,

$$\Delta_2(t) = 4 \int_0^t d\tau (t-\tau) \langle \mathcal{D}_{\parallel}(\tau) \rangle \cong 4t \int_0^{\infty} \langle \mathcal{D}_{\parallel}(\tau) \rangle .$$

At time scales longer than the NGP peak time, $L(z)$ in eq 1 can be approximated by the following Smoluchowski operator, i.e., $L(z) \cong L_{\text{SM}}(z) = \partial_z [D_{\perp}(z)(\partial_z + \partial_z \beta U(z))]$. Here, $D_{\perp}(z)$ and $\beta U(z)$, respectively, denote the z -dependent diffusion coefficient associated with the thermal motion of water molecules in the direction perpendicular to the membrane and the thermal energy-scaled potential of mean force with $\beta = 1/k_B T$. k_B and T denote the Boltzmann constant and temperature, respectively. After the onset of the Fickian diffusion, the MSD and NGP of the lateral diffusion of water molecules assume the following analytic forms:

$$\Delta_2(t) \cong 4 \langle D_{\parallel} \rangle t, \quad (4a)$$

$$\alpha_2(t) \cong \frac{2\eta_D^2}{t^2} \int_0^t dt' (t-t') \phi_D(t'). \quad (4b)$$

In eq 4, $\langle D_{\parallel} \rangle$ and $\eta_D^2 [= \langle \delta D_{\parallel}^2 \rangle / \langle D_{\parallel} \rangle^2]$ denote, respectively, the mean diffusion coefficient defined by $\langle D_{\parallel} \rangle = \int_0^{\infty} \langle \mathcal{D}_{\parallel}(\tau) \rangle$ and the relative variance of the z -dependent lateral diffusion coefficient, with δf denoting the deviation of a quantity f from its mean, i.e., $\delta f(z) = f(z) - \langle f \rangle$. $\phi_D(t)$ denotes the normalized time-correlation function (TCF) of the lateral diffusion coefficient fluctuation, i.e.,

$$\phi_D(t) = \frac{\langle \delta D_{\parallel}(t) \delta D_{\parallel}(0) \rangle}{\langle \delta D_{\parallel}^2 \rangle} = \langle \delta D_{\parallel}^2 \rangle^{-1} \int_0^{\ell} dz \int_0^{\ell} dz_0 \delta D_{\parallel}(z) G_{\text{SM}}(z, t | z_0) \delta D_{\parallel}(z_0) P_{eq}(z_0), \quad (5)$$

where $G_{\text{SM}}(z, t | z_0)$ designates Green's function of Smoluchowski equation governing the thermal motion of water molecules in the direction perpendicular to the membranes, i.e., $\partial_t G_{\text{SM}}(z, t | z_0) = L_{\text{SM}}(z) G_{\text{SM}}(z, t | z_0)$, with the initial condition, $G_{\text{SM}}(z, 0 | z_0) = \delta(z - z_0)$.

Equations 4b and 5 indicate that, for nanoconfined water molecules, the non-Gaussian diffusion in the lateral direction originates from fluctuation of the lateral diffusion coefficient coupled to water motion in the longitudinal direction. We note here that the DKC defined in eq 3 reduces to $\eta_D^2 \phi_D(t)$ at long times where the MSD linearly increases with time; the long-time profile of $C_D(t)$ extracted from the MSD and NGP time profiles of our MD simulation results is in quantitative agreement with our theoretical result for $\eta_D^2 \phi_D(t)$ calculated using eq (5) (Figure 4a). This agreement between simulation and theory supports the validity of our assumption underlying eq (1) that the dynamic fluctuation in the lateral diffusion coefficient of water molecules primarily originates from its coupling to the thermal motion of water molecules in the longitudinal direction. We also performed MD simulation study on the thermal motion of water molecules in the intermembrane space, for a system of SPC/E water molecules confined between two lipid bilayers, each composed of 128 DMPC molecules, systematically changing the ratio of the number of water molecules to the number of lipid molecules and the distance ℓ between the two membrane centers (Figure 1). We employed the AMBER lipid 14 force field for simulation of the lipid molecules²⁶ and imposed periodic boundary conditions on the system. We also investigated the transport dynamics of a pure, bulk water system, using the MD simulation of 5000 SPC/E water molecules, and compared it to the transport dynamics of the nanoconfined water molecules. Our MD

simulation was conducted for a system at a temperature of 318 K in the NVT ensemble. Additional information about the simulations can be found in the Supporting Information.

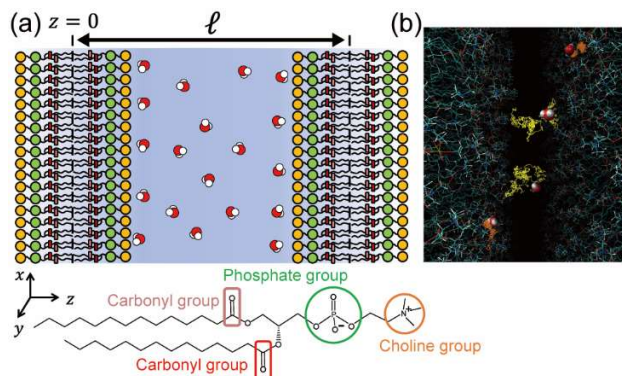


Figure 1. (a) Schematic representation of our MD simulation system: water molecules confined between two DMPC lipid bilayers. The simulation was performed for the system with three different intermembrane separations, i.e., $\ell = 53.2 \text{ \AA}$, 61.8 \AA , and 80.6 \AA . (b) Representative trajectories of water molecules undergoing thermal motion between the lipid bilayers for 50 ps: (yellow lines) the trajectories of water molecules freely moving near the center of the intermembrane space, (orange lines) trajectories of water molecules strongly interacting with the lipid head groups of DMPC.

From the MD simulation trajectories of water molecules, we obtained the MSD and NGP of the lateral water displacement for each system (Figure 2). The time profile of the MSD obtained from the MD simulation exhibits a dynamic transition behavior that is dependent on the separation between the two lipid membranes (Figure 2a). The time profile of the MSD shows the transition from an initial ballistic motion ($\Delta_2(t) \sim t^2$) to terminal Fickian diffusion ($\Delta_2(t) \sim t^1$), with intermediate subdiffusion ($\Delta_2(t) \sim t^\alpha$ with $0 < \alpha < 1$). The short-time ballistic behavior of the

MSD shows little variation with changes in ℓ and quadratically increases with time, i.e., $\Delta_2(t) = 2k_B T t^2 / M$ ²³. Here, M denotes the mass of a water molecule. However, the intermediate subdiffusive regime becomes more pronounced, and the value of long-time lateral diffusion coefficient gets smaller as the separation, ℓ , between lipid bilayers decreases. These findings align with previous studies^{10,12,16,21}. The time profiles of the MSD could be quantitatively explained by using the analytic formula for the MSD of a bead in a Gaussian polymer, shown as solid lines in Figure 2a²³.

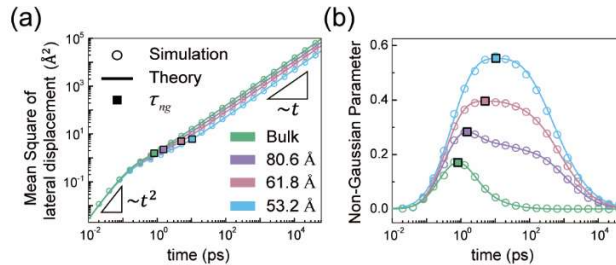


Figure 2. (a) Mean square displacement (MSD) and (b) non-Gaussian parameter (NGP) associated with the lateral displacement of water molecules for systems with various intermembrane separations: (circles) simulation results (solid lines) eq S19 for MSD and eq S21 for NGP (square) the NGP peak time (τ_{ng})

Our MD simulation study reveals that both the NGP peak time and the peak height increase as the separation, ℓ , between the membranes decreases (Figure 2b). A longer peak time and a greater peak height of the NGP signify, respectively, prolonged trapping of water molecules^{23,27} and increased fluctuation in the lateral diffusion coefficient (see eq 4b and Figure 4a). These phenomena can be attributed to the attractive interactions between interfacial water molecules and the functional groups in the lipid molecules. As ℓ decreases, the proportion of the trapped

interfacial water molecules grows, leading to a decrease in the mean lateral diffusion coefficient and an increase in the variance of the diffusion coefficient.

At times longer than the NGP peak time, the nanoconfined molecules undergo Fickian yet non-Gaussian diffusion, with the NGP value decreasing with time. The nanoconfined water molecules have a far greater NGP value than bulk water molecules. The NGP of bulk water molecules becomes negligible at times longer than 10 ps; in contrast, the NGP of the nanoconfined water molecules does not vanish at times longer than 10 ns. The NGP shows a strongly non-exponential relaxation dynamics, whose time profile can be quantitatively explained by eqs 4b and 5 as shown later in this Letter.

We then identify the interfacial region where water molecules directly interact with the lipid head groups. For this purpose, we investigate the structure and dynamics of water molecules near the lipid-bilayers using the MD simulations. Figures 3a and 3b show the z -dependence of the density profile, $\rho(z)$, and the dipole orientation profile, $\langle \cos \theta \rangle_z$, of the nanoconfined water. Here, θ and bracket $\langle \dots \rangle_z$ denote the angle between the water dipole moment and the z -axis and the average over water molecules located within an interval $(z-0.25 \text{ \AA}, z+0.25 \text{ \AA})$, respectively. As shown in Figure 3a, the water molecules in close vicinity of the membrane exhibit a lower density compared to the density, $\rho_{bulk}^{45^\circ C} = 0.99 \text{ g}\cdot\text{cm}^{-3}$, of bulk water²⁸. The dipole orientation profile, $\langle \cos \theta \rangle_z$, does not vanish for water molecules in the vicinity of the functional groups in the lipid molecules. This results from the non-isotropic interactions between the water molecules and those functional groups, whose positions along the z -direction are shown in Figure 3a. At positions near $z \cong 20 \text{ \AA}$, $\langle \cos \theta \rangle_z$ has a negative value, while at positions near $z \cong \ell - 20 \text{ \AA}$, it has a positive value, indicating that the water dipole moment tends to point toward phosphate and carbonyl

groups rather than choline groups^{7,8}. This is because water molecules in the vicinity of phosphate and carbonyl groups experience strong restrictions on their orientations due to the hydrogen bonding with these groups, whereas those near choline groups exhibit broadly distributed angle distribution, forming the clathrate-like hydration shell around the choline groups^{4,13}

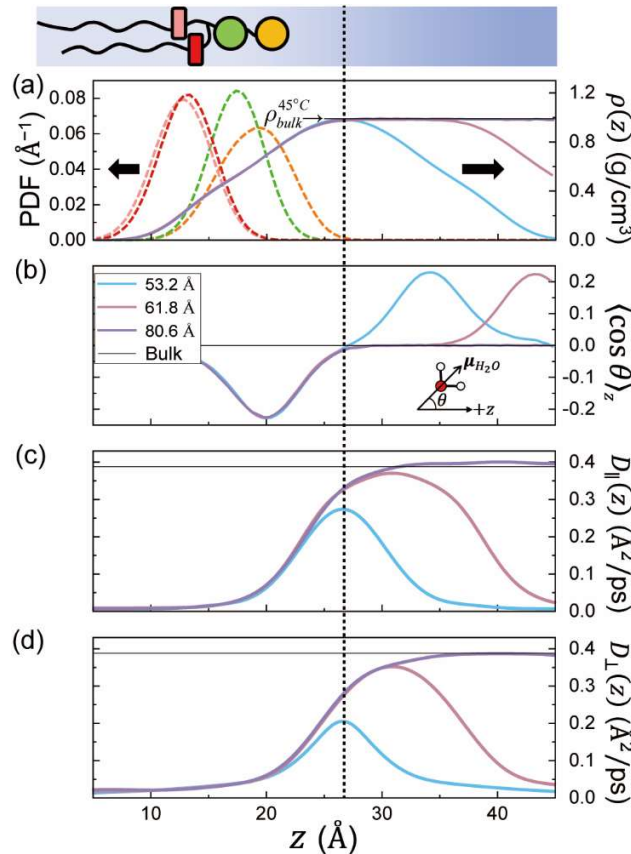


Figure 3. Dependence of structural and dynamical properties of the water molecules on the distance z from the center of the lipid membrane in the left. z -dependent profile of (a) mass density, $\rho(z)$, (b) orientation $\langle \cos \theta \rangle_z$, (c) lateral diffusion coefficient, $D_{||}(z)$, and (d) longitudinal diffusion coefficient, $D_{\perp}(z)$, of water molecules. θ designates the angle between the water moment and the longitudinal axis. (dotted line) the position of the boundary, $z_c = 26.6 \text{ \AA}$, between interfacial water region and bulk-like water region. (dashed lines) probability distribution of the

positions of various functional groups in the DMPC: (orange) the nitrogen atom in the choline group (green) phosphorus atom in the phosphate group (red and pink) the oxygen atoms in the two carbonyl groups. The probability distribution of these functional groups as well as the z -dependent profiles of $\rho(z)$ and $\langle \cos \theta \rangle_z$ are largely independent of the intermembrane separation.

Remarkably, the density and dipole orientation profiles show little dependence on ℓ for the interfacial water molecules at z smaller than $z_c = 26.6 \text{ \AA}$ but recover their respective bulk-limit values in the intermediate region defined by $z_c \leq z \leq \ell - z_c$. Based on these observations, we define z_c as the boundary between the interfacial water region and the bulk-like water region. The value of z_c ($= 26.6 \text{ \AA}$) estimated from our MD simulation is found to be comparable to the previously reported z_c values, 24 \AA and 28 \AA , which were estimated by investigating the structural order¹⁵ and the rotational dynamics¹⁹ of water molecules near the lipid membrane.

The diffusion coefficients of water molecules are also strongly dependent on their distance from the membrane. We obtain the z -dependent profiles of $D_{\parallel}(z)$ and $D_{\perp}(z)$ using umbrella sampling and mean first passage time analysis, respectively^{14,29}. Within the interfacial water region ($z < z_c$), both the diffusion coefficients increase with z , and their z -dependent profiles are also similar across various intermembrane separations. For the system with $\ell = 80.6 \text{ \AA}$, both diffusion coefficients recover the bulk-limit value, $D_{bulk}^{45^\circ C} = 3.88 \times 10^{-1} \text{ \AA}^2 \cdot \text{ps}^{-1}$, of the SPC/E water at distances greater than z_c . However, for the systems with $\ell < 80.6 \text{ \AA}$, the values of $D_{\parallel}(z)$ and $D_{\perp}(z)$ are smaller than $D_{bulk}^{45^\circ C}$ across the entire z region. For example, when the value of ℓ is 53.2 \AA , the maximum values of $D_{\parallel}(\ell/2)$ and $D_{\perp}(\ell/2)$ are only about 70% and 50% of $D_{bulk}^{45^\circ C}$, respectively. Noting that

the longitudinal position, z , of the central nitrogen atom in the choline group is about $19.3 \pm 4 \text{ \AA}$ (Figure 3a), these results suggest that the choline group in the lipid molecule retard the translational motion of water molecules located beyond its first hydration shell, which extends about 4.5 \AA from the central nitrogen atom in the choline group¹³.

The z -dependence profiles of water density $\rho(z)$ and the diffusion coefficients, $D_{\parallel}(z)$ and $D_{\perp}(z)$, are related to the time profile of $\eta_D^2 \phi_D(t)$ and the NGP according to eqs 4b and 5. Equation 4b tells us that, after the onset of Fickian diffusion, the NGP time profile is completely determined by the mean-scaled TCF, $\eta_D^2 \phi_D(t) = \langle \delta D_{\parallel}(t) \delta D_{\parallel}(0) \rangle / \langle D_{\parallel} \rangle^2$, of the diffusion coefficient fluctuation.

Here, $\eta_D^2 = \langle D_{\parallel}^2 \rangle / \langle D_{\parallel} \rangle^2 - 1$ can be calculated from $D_{\parallel}(z)$ and $\rho(z)$ by using

$$\langle D_{\parallel}^n \rangle = \int_0^{\ell} dz D_{\parallel}^n(z) P_{eq}(z) \text{ with } P_{eq}(z) = \rho(z) / \int_0^{\ell} dz \rho(z). \phi_D(t) \text{ can also be calculated from eq}$$

(5), where the Green's function $G_{SM}(z, t | z_0)$ is obtained by solving $\partial_t G_{SM}(z, t | z_0)$

$$= \partial_z [D_{\perp}(z)(\partial_z + \partial_z \beta U(z))] G_{SM}(z, t | z_0) \text{ with the initial condition } G_{SM}(z, 0 | z_0) = \delta(z - z_0). \text{ The}$$

thermal energy-scaled potential of mean force, $\beta U(z)$, can be estimated from $\rho(z)$ by $\beta U(z)$

$$= -\ln[\rho(z) / \rho_{bulk}^{45^\circ C}]. \text{ Across systems with various intermembrane separations, the result of}$$

$\eta_D^2 \phi_D(t)$ calculated using our theory closely matches the long-time profile of $C_D(t)$ directly

extracted from the MD simulation results (Figure 4a). In addition, the NGP time profiles calculated

from eq 4b are also in quantitative agreement with the MD simulation results (Figure 4b).

Furthermore, our theory predicts the lateral displacement distribution with a unimodal peak and a

non-Gaussian tail for nanoconfined water molecules. We find the prediction of our theory in

excellent agreement with the MD simulation results for the time-dependent lateral displacement

distribution of water molecules at various times and separations between the membranes (Figure

4c). The agreement between theory and simulation again demonstrates the validity of our assumption underlying eq 1, that is, the most important variable that affects the lateral thermal motion of an interfacial water molecule is the distance, z , between a water molecule and the center of the membrane.

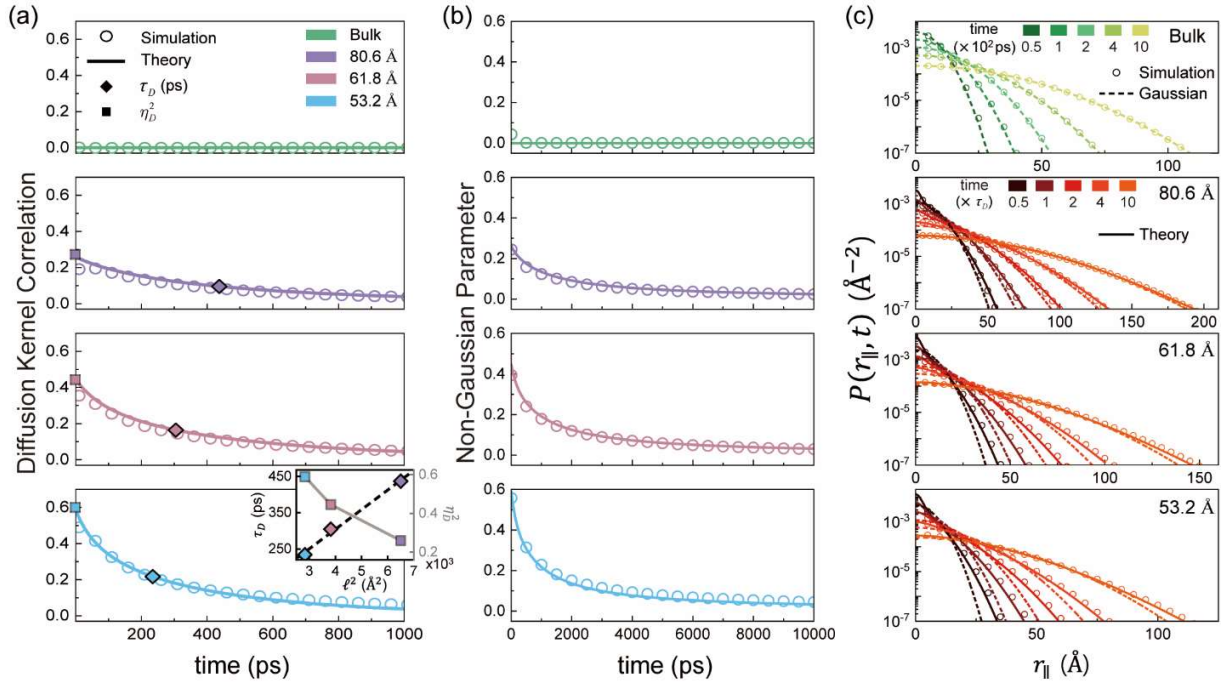


Figure 4. Diffusion Kernel Correlation, Non-Gaussian Parameter, and Lateral Displacement Distribution of water molecules confined between two lipid membranes with various intermembrane separations. (a) Comparison between the diffusion kernel correlation and the mean-scaled time correlation function of the lateral diffusion coefficient fluctuation: (circles) Diffusion Kernel Correlation, $C_D(t)$, from the MD simulation results (solid lines) mean-scaled TCFs, $\eta_D^2 \phi_D(t)$, of the lateral diffusion coefficient fluctuation calculated by eq 5 (diamond) relaxation time τ_D defined by $\phi_D(\tau_D) = e^{-1}$ (square) the value of the relative variance, η_D^2 , of the diffusion coefficient (Inset in (a)) Dependence of τ_D and η_D^2 on the square, ℓ^2 , of intermembrane

separation (b) Non-Gaussian parameter $\alpha_2(t)$: (circles) simulation (solid line) eq 4b. (c) Lateral displacement distributions at various times: (circles) simulation results (solid lines) theoretical predictions (dotted line) Gaussian with zero mean and variance given by $4\langle D_{\parallel} \rangle t$.

The relaxation time τ_D of $\phi_D(t)$, defined by $\phi_D(\tau_D) = e^{-1}$, quadratically increases with the intermembrane separation ℓ (see inset of Figure 4a). This follows because, for the complete relaxation of the diffusion coefficient fluctuation, water molecules must travel the entire intermembrane space, and the time taken for this process should be proportional to the mean first passage time, which quadratically increases with ℓ (Movie S1). On the other hand, η_D^2 decreases with ℓ . This is because, as ℓ increases, the proportion of the trapped interfacial water molecules decreases, which leads to an increase in the mean lateral diffusion coefficient and a decrease in the variance of the diffusion coefficient.

We note here that, at times shorter than 0.1 ps, the NGP increases with time, which cannot be explained by eq 4b. At such short times, the DKC can be approximated by $C_D(t) \cong 2\left[\langle \mathcal{D}_{\parallel}(t) \rangle / \langle \mathcal{D}_{\parallel}(0) \rangle\right]^2 = 2\phi_v^2(t)$ (see the Figure S3a in the Supporting Information), where $\phi_v(t)$ denotes the normalized VAF of water molecules. Using this approximation in eq 2, we obtained the following short-time asymptotic expression of the NGP as

$$\alpha_2(t) = \frac{1}{18}(\gamma^2 - \mu)t^2 + \mathcal{O}(t^3), \quad (6)$$

where γ and μ denote $-\lim_{t \rightarrow 0} \partial \phi_v(t) / \partial t$ and $\lim_{t \rightarrow 0} \partial^2 \phi_v(t) / \partial t^2$, respectively. Explicit expressions of γ and μ are available for our model (see the paragraph below eq M24 in the Supporting

Information). According to this result, the NGP quadratically increases with time, which quantitatively explains our simulation results for the short-time asymptotic behavior of the NGP.

The major contributor to the short-time dynamics of the NGP is the relaxation dynamics of the velocity fluctuation, and the two-time velocity auto-correlation function completely determines the NGP time profile. After the onset of Fickian diffusion, however, the relaxation dynamics of the diffusion coefficient fluctuation additionally contributes to the NGP time profile. For bulk water system, where the diffusion coefficient fluctuation is negligible, the short-time asymptotic expression of the NGP that only accounts for the velocity relaxation provides a quantitative explanation of the long-time relaxation of the NGP as well as the short-time relaxation (see the Figure S3b in the Supporting Information).

We present a physical model and transport equation that quantitatively explain the stochastic thermal motion of water molecules in intermembrane space. The lateral displacement distribution of the water molecules nanoconfined between two membranes strongly deviates from Gaussian, which originates from dynamic fluctuation in the lateral diffusion coefficient. This fluctuation occurs because the lateral diffusion coefficient of a water molecule primarily depends on its distance from the membrane center, and this distance fluctuates over time, owing to thermal motion of the water molecule in the longitudinal direction. In addition, using the molecular dynamics (MD) simulation, we investigate the dependence of the mass density, the orientation, and the lateral and longitudinal diffusion coefficients of a water molecule nanoconfined between two phospholipid membranes on its distance from the phospholipid membrane center. This study shows the presence of interfacial region within 26.6 Å from the membrane center. Water molecules in the interfacial region have a structure and dynamics far different from bulk water molecules. The properties of interfacial water molecules are robust with respect to changes in intermembrane

separation. Our theory provides a unified, quantitative explanation of our MD simulation results for the mean square displacement, non-Gaussian parameter, and displacement distribution of nanoconfined water molecules. Our model is applicable or can be extended to quantitative investigation into the dynamics of transport and transport-coupled processes occurring in various nanoconfined environments.

ASSOCIATED CONTENT

Supporting Information

Movie S1: Heatmap of discrete Green's function (MP4)

Additional figures, tables, computational details for MD simulation and captions for Movie S1 (PDF)

ACKNOWLEDGMENT

This work was supported by the Institute for Basic Science (IBS-R023-D1), the Creative Research Initiative Project program (2015R1A3A2066497) funded by the National Research Foundation (NRF) of Korea, and the NRF grants (NRF-2020R1A2C1102788 and RS-2023-00245431) funded by Korea government (MSIT).

REFERENCES

- (1) Demirel, Y.; Gerbaud, V. Chapter 11 - Thermodynamics and Biological Systems. In *Nonequilibrium Thermodynamics (Fourth Edition)*; Demirel, Y., Gerbaud, V., Eds.; Elsevier, 2019; pp 489–571. <https://doi.org/https://doi.org/10.1016/B978-0-444-64112-0.00011-3>.
- (2) McCann, F. E.; Vanherberghen, B.; Eleme, K.; Carlin, L. M.; Newsam, R. J.; Goulding, D.; Davis, D. M. The Size of the Synaptic Cleft and Distinct Distributions of Filamentous Actin, Ezrin, CD43, and CD45 at Activating and Inhibitory Human NK Cell Immune Synapses. *The Journal of Immunology* **2003**, *170* (6), 2862–2870. <https://doi.org/10.4049/jimmunol.170.6.2862>.
- (3) Terasaki, M.; Shemesh, T.; Kasthuri, N.; Klemm, R. W.; Schalek, R.; Hayworth, K. J.; Hand, A. R.; Yankova, M.; Huber, G.; Lichtman, J. W.; Rapoport, T. A.; Kozlov, M. M. Stacked Endoplasmic Reticulum Sheets Are Connected by Helicoidal Membrane Motifs. *Cell* **2013**, *154* (2), 285–296. <https://doi.org/10.1016/j.cell.2013.06.031>.
- (4) Zhao, W.; Moilanen, D. E.; Fenn, E. E.; Fayer, M. D. Water at the Surfaces of Aligned Phospholipid Multibilayer Model Membranes Probed with Ultrafast Vibrational Spectroscopy. *J Am Chem Soc* **2008**, *130* (42), 13927–13937. <https://doi.org/10.1021/ja803252y>.
- (5) Kundu, A.; Kwak, K.; Cho, M. Water Structure at the Lipid Multibilayer Surface: Anionic Versus Cationic Head Group Effects. *J Phys Chem B* **2016**, *120* (22), 5002–5007. <https://doi.org/10.1021/acs.jpccb.6b02340>.
- (6) Kundu, A.; Błasiak, B.; Lim, J.-H.; Kwak, K.; Cho, M. Water Hydrogen-Bonding Network Structure and Dynamics at Phospholipid Multibilayer Surface: Femtosecond Mid-IR Pump–Probe Spectroscopy. *J Phys Chem Lett* **2016**, *7* (5), 741–745. <https://doi.org/10.1021/acs.jpcllett.6b00022>.
- (7) Mondal, J. A.; Nihonyanagi, S.; Yamaguchi, S.; Tahara, T. Three Distinct Water Structures at a Zwitterionic Lipid/Water Interface Revealed by Heterodyne-Detected Vibrational Sum Frequency Generation. *J Am Chem Soc* **2012**, *134* (18), 7842–7850. <https://doi.org/10.1021/ja300658h>.
- (8) Dreier, L. B.; Wolde-Kidan, A.; Bonthuis, D. J.; Netz, R. R.; Backus, E. H. G.; Bonn, M. Unraveling the Origin of the Apparent Charge of Zwitterionic Lipid Layers. *J Phys Chem Lett* **2019**, *10* (20), 6355–6359. <https://doi.org/10.1021/acs.jpcllett.9b02587>.
- (9) Zhang, R.; Cross, T. A.; Peng, X.; Fu, R. Surprising Rigidity of Functionally Important Water Molecules Buried in the Lipid Headgroup Region. *J Am Chem Soc* **2022**, *144* (17), 7881–7888. <https://doi.org/10.1021/jacs.2c02145>.
- (10) Kazoe, Y.; Mawatari, K.; Li, L.; Emon, H.; Miyawaki, N.; Chinen, H.; Morikawa, K.; Yoshizaki, A.; Dittrich, P. S.; Kitamori, T. Lipid Bilayer-Modified Nanofluidic Channels of Sizes with Hundreds of Nanometers for Characterization of Confined Water and

- Molecular/Ion Transport. *J Phys Chem Lett* **2020**, *11* (14), 5756–5762. <https://doi.org/10.1021/acs.jpcllett.0c01084>.
- (11) Saruko, T.; Morikawa, K.; Kitamori, T.; Mawatari, K. Proton Diffusion and Hydrolysis Enzymatic Reaction in 100 Nm Scale Biomimetic Nanochannels. *Biomicrofluidics* **2022**, *16* (4), 044109. <https://doi.org/10.1063/5.0105297>.
 - (12) Kazoe, Y.; Ikeda, K.; Mino, K.; Morikawa, K.; Mawatari, K.; Kitamori, T. Quantitative Characterization of Liquids Flowing in Geometrically Controlled Sub-100 Nm Nanofluidic Channels. *Analytical Sciences* **2023**. <https://doi.org/10.1007/s44211-023-00311-x>.
 - (13) Lee, E.; Kundu, A.; Jeon, J.; Cho, M. Water Hydrogen-Bonding Structure and Dynamics near Lipid Multibilayer Surface: Molecular Dynamics Simulation Study with Direct Experimental Comparison. *J Chem Phys* **2019**, *151* (11), 114705. <https://doi.org/10.1063/1.5120456>.
 - (14) von Hansen, Y.; Gekle, S.; Netz, R. R. Anomalous Anisotropic Diffusion Dynamics of Hydration Water at Lipid Membranes. *Phys Rev Lett* **2013**, *111* (11), 118103. <https://doi.org/10.1103/PhysRevLett.111.118103>.
 - (15) Martelli, F.; Crain, J.; Franzese, G. Network Topology in Water Nanoconfined between Phospholipid Membranes. *ACS Nano* **2020**, *14* (7), 8616–8623. <https://doi.org/10.1021/acsnano.0c02984>.
 - (16) Högberg, C.-J.; Lyubartsev, A. P. A Molecular Dynamics Investigation of the Influence of Hydration and Temperature on Structural and Dynamical Properties of a Dimyristoylphosphatidylcholine Bilayer. *J Phys Chem B* **2006**, *110* (29), 14326–14336. <https://doi.org/10.1021/jp0614796>.
 - (17) Yamamoto, E.; Akimoto, T.; Hirano, Y.; Yasui, M.; Yasuoka, K. Power-Law Trapping of Water Molecules on the Lipid-Membrane Surface Induces Water Retardation. *Phys Rev E Stat Nonlin Soft Matter Phys* **2013**, *87* (5), 052715. <https://doi.org/10.1103/PhysRevE.87.052715>.
 - (18) Hansen, F. Y.; Peters, G. H.; Taub, H.; Miskowicz, A. Diffusion of Water and Selected Atoms in DMPC Lipid Bilayer Membranes. *J Chem Phys* **2012**, *137* (20), 204910. <https://doi.org/10.1063/1.4767568>.
 - (19) Martelli, F.; Ko, H.-Y.; Borallo, C. C.; Franzese, G. Structural Properties of Water Confined by Phospholipid Membranes. *Front Phys (Beijing)* **2017**, *13* (1).
 - (20) Malik, S.; Debnath, A. Dehydration Induced Dynamical Heterogeneity and Ordering Mechanism of Lipid Bilayers. *J Chem Phys* **2021**, *154* (17), 174904. <https://doi.org/10.1063/5.0044614>.
 - (21) Calero, C.; Stanley, H.; Franzese, G. Structural Interpretation of the Large Slowdown of Water Dynamics at Stacked Phospholipid Membranes for Decreasing Hydration Level: All-Atom Molecular Dynamics. *Materials* **2016**, *9* (5), 319. <https://doi.org/10.3390/ma9050319>.

- (22) Wang, B.; Kuo, J.; Bae, S. C.; Granick, S. When Brownian Diffusion Is Not Gaussian. *Nat Mater* **2012**, *11* (6), 481–485. <https://doi.org/10.1038/nmat3308>.
- (23) Song, S.; Park, S. J.; Kim, M.; Kim, J. S.; Sung, B. J.; Lee, S.; Kim, J.-H.; Sung, J. Transport Dynamics of Complex Fluids. *Proceedings of the National Academy of Sciences* **2019**, *116* (26), 12733–12742. <https://doi.org/10.1073/pnas.1900239116>.
- (24) Rahman, A.; Singwi, K. S.; Sjölander, A. Theory of Slow Neutron Scattering by Liquids. I. *Physical Review* **1962**, *126* (3), 986–996. <https://doi.org/10.1103/PhysRev.126.986>.
- (25) Rahman, A. Correlations in the Motion of Atoms in Liquid Argon. *Physical Review* **1964**, *136* (2A), A405–A411. <https://doi.org/10.1103/PhysRev.136.A405>.
- (26) Dickson, C. J.; Madej, B. D.; Skjerve, Å. A.; Betz, R. M.; Teigen, K.; Gould, I. R.; Walker, R. C. Lipid14: The Amber Lipid Force Field. *J Chem Theory Comput* **2014**, *10* (2), 865–879. <https://doi.org/10.1021/ct4010307>.
- (27) Odagaki, T.; Hiwatari, Y. Gaussian-to-Non-Gaussian Transition in Supercooled Fluids. *Phys Rev A (Coll Park)* **1991**, *43* (2), 1103–1106. <https://doi.org/10.1103/PhysRevA.43.1103>.
- (28) Wagner, W.; Pruß, A. The IAPWS Formulation 1995 for the Thermodynamic Properties of Ordinary Water Substance for General and Scientific Use. *J Phys Chem Ref Data* **2002**, *31* (2), 387–535. <https://doi.org/10.1063/1.1461829>.
- (29) Szabo, A.; Schulten, K.; Schulten, Z. First Passage Time Approach to Diffusion Controlled Reactions. *J Chem Phys* **1980**, *72* (8), 4350–4357. <https://doi.org/10.1063/1.439715>.

1 **Supporting Information for**

2 **Transport Dynamics of Water Molecules**

3 **Confined between Lipid Membranes**

4 Minho Lee^{1,2}, Euihyun Lee³, Ji-hyun Kim^{1,2}, Hyunseok Hwang⁶, Minhaeng Cho^{4,5*}, and Jaeyoung Sung^{1,2*}

5 *¹ Creative Research Initiative Center for Chemical Dynamics in Living Cells, Chung-Ang University, Seoul*
6 *06974, Republic of Korea*

7 *² Department of Chemistry, Chung-Ang University, Seoul 06974, Republic of Korea*

8 *³ Department of Chemistry, The University of Texas at Austin, TX 78757, USA*

9 *⁴ Center for Molecular Spectroscopy and Dynamics, Institute for Basic Science (IBS), Seoul 02841, Republic of*
10 *Korea*

11 *⁵ Department of Chemistry, Korea University, Seoul 02841, Republic of Korea*

12 *⁶ Department of Chemistry, Institute for Molecular Science and Fusion Technology, Kangwon National*
13 *University, Chuncheon, Gangwon-do 24341, Republic of Korea*

14 Corresponding authors: jaeyoung@cau.ac.kr (J.S.), mcho@korea.ac.kr (M.C.)

15	Table of contents	
16		
17	Computational details: Molecular Dynamics Simulations	3
18	Derivation of analytic expressions for the MSD and NGP.....	6
19	Figure S1: z-dependent profiles of lateral diffusion coefficient.....	11
20	Figure S2: z-dependent profiles of longitudinal diffusion coefficient.....	15
21	Figure S3: Diffusion Kernel Correlation and Non-Gaussian Parameter	17
22	Figure S4: Relationship between DKC and NGP at long times	20
23	Movie S1: Heatmap of discrete Green's function.....	21
24	Supplemental Tables	23
25	Reference.....	26
26		
27		

28 Computational details: Molecular Dynamics Simulations

29 Molecular Dynamics (MD) simulations were carried out using the AMBER 21 program
30 package. We constructed simulation systems composed of 128 DMPC (1,2-dimyristoyl-sn-
31 glycerol-3-phosphocholine) lipids and a various number, 2560, 3840, and 6400 of water
32 molecules, using the CHARMM-GUI membrane builder tool¹⁻⁶. The force field parameters of
33 DMPC and water molecules were replaced with the AMBER lipid 14⁷ and SPC/E, respectively.
34 Similarly, an MD simulation system for pure water, which is composed of 5,000 water
35 molecules, was constructed using CHARMM-GUI solution builder^{1,2,6}, and the MD simulation
36 was carried out using the same SPC/E force field. Periodic boundary conditions were applied
37 to both the pure water and the lipid bilayer systems. In the case of the pure water system, our
38 pure water model system with the periodic boundary conditions serves as a realistic and reliable
39 representation of bulk water without edge effects. For the lipid bilayer system, our periodic
40 boundary conditions effectively confine the water molecules within the lipid membranes. The
41 particle mesh Ewald method⁸ was used to calculate long-range electrostatic interactions, and
42 the cutoff distance of 10 Å was used to calculate the Lennard-Jones interaction and the real
43 space part of the Ewald sum. A time step of our MD simulations was set to 1 fs.

44 Before obtaining the simulation trajectories of the NVT ensemble of our systems, we
45 conducted an equilibration procedure. For the pure water simulation, the initial configuration
46 of water molecules was first stabilized through energy minimization for 5,000 steps, employing
47 both the steepest descent method and the conjugate gradient method. This was followed by a 2
48 ns constant NpT equilibration at 1.0 atm and 318 K, using isotropic position scaling with a
49 relaxation time of 2 ps. For temperature control, the Langevin thermostat, with a collision
50 frequency of 1.0 ps⁻¹, was utilized. Subsequently, a 2 ns constant NVT simulation at 318 K was
51 carried out, using the Langevin thermostat to ensure that the system relaxed to the thermal

52 equilibrium state. Regarding the DMPC lipid bilayer system simulation, the initial
53 configuration of the system underwent a 10,000-step energy minimization using both the
54 steepest descent method and the conjugate gradient method. Then, the system was rapidly
55 heated from 0 K to 100 K over 40 ps, using the Langevin thermostat with a collision frequency
56 of 1.0 ps^{-1} and weak restraints on the lipid molecules with a force constant of $10. \text{ kcal mol}^{-1}$
57 \AA^{-2} . Subsequently, a gradual heating from 100 K to 318 K over 2 ns was performed with the
58 same thermostat setting and restraints. After the heating process, a 50 ns NpT simulation was
59 carried out at 318 K, using the Langevin thermostat with anisotropic pressure scaling (1 atm)
60 without restraining lipids. From the results of the last process, the values of the separation, ℓ ,
61 between two lipid membranes, i.e., system box length along the perpendicular direction to the
62 membrane surface, were determined. The values of the intermembrane separations, ℓ , are 53.2
63 \AA , 61.8 \AA , and 80.6 \AA for our DMPC lipids simulation systems containing 2560, 3840, and
64 6400 water molecules, respectively.

65 After the equilibration procedure, production runs were carried out for our systems at 318
66 K under constant NVT conditions with the following procedures:

67 (1) To calculate the mean square displacement (MSD) and non-Gaussian parameter (NGP)
68 for the lateral displacement of water molecules, shown in Figure 2, we conducted the
69 MD simulation for each system using two different recording time intervals. The
70 simulation trajectories were recorded every 10 fs for the first 1 ns-long NVT
71 simulations to investigate the short-time dynamics of water molecules. Afterward, the
72 trajectories were saved every 10 ps over the following 99 ns-long NVT simulation to
73 investigate the long-time dynamics of the system. This 1 ns-long NVT simulations
74 were repeated seven times for each intermembrane separation of our system.

75 (2) To obtain the z-dependent profile of the lateral diffusion coefficient, $D_{\parallel}(z)$, shown in

76 Figure S1, we conducted additional simulation runs using umbrella sampling. The
77 simulation trajectories were recorded at every 10 ps during the 1 μ s-long *NVT*
78 simulations. A more detailed description of this simulation process is presented in the
79 caption of Figure S1.

80 (3) To obtain the *z*-dependent profile, the longitudinal diffusion coefficient, $D_{\perp}(z)$,
81 profiles shown in Figure S2, using the method presented in Ref.⁹⁻¹¹, we conducted
82 another set of simulations where the simulation trajectories were saved at intervals of
83 1 ps for the 1 μ s-long *NVT* simulations. A more detailed description of this simulation
84 is presented in the caption of Figure S2.

85 Derivation of analytic expressions for the MSD and NGP

86 Let us first obtain the analytic expression for the second and fourth moments of the lateral
 87 displacement of water molecules in the intermembrane space, starting from eq 1. On the left-
 88 hand-side of eq 1, $\hat{p}(\mathbf{r}_{\parallel}, z, s)$ can be replaced by $\hat{p}(\mathbf{r}_{\parallel}, z, s) = s\hat{p}(\mathbf{r}_{\parallel}, z, s) - p(\mathbf{r}_{\parallel}, z, 0)$. Here,
 89 $p(\mathbf{r}_{\parallel}, z, 0)$ denotes the initial condition of the joint probability density, given by $p(\mathbf{r}_{\parallel}, z, 0)$
 90 $= \delta(\mathbf{r}_{\parallel} - \mathbf{r}_{\parallel,0})P_{eq}(z)$, where, $\mathbf{r}_{\parallel,0}$ and $P_{eq}(z)$ denote the initial lateral position vector and the
 91 equilibrium distribution of water molecule along the z -axis, respectively. When $\mathbf{r}_{\parallel,0}$ is chosen
 92 to be the origin of our coordinate, i.e., $\mathbf{r}_{\parallel,0} = \mathbf{0}$, \mathbf{r}_{\parallel} represents the displacement vector. By
 93 taking the Fourier transform of eq 1, we obtain

$$94 \quad \hat{\dot{p}}(\mathbf{k}_{\parallel}, z, s) = s\hat{p}(\mathbf{k}_{\parallel}, z, s) - P_{eq}(z) = -\hat{\mathcal{D}}_{\parallel}(z, s)k_{\parallel}^2 \hat{p}(\mathbf{k}_{\parallel}, z, s) + L(z)\hat{p}(\mathbf{k}_{\parallel}, z, s). \quad (\text{S1})$$

95 Here, $\hat{p}(\mathbf{k}_{\parallel}, z, s)$ and k_{\parallel} represent the Fourier transformation of $\hat{p}(\mathbf{r}_{\parallel}, z, s)$, defined by
 96 $\hat{p}(\mathbf{k}_{\parallel}, z, s) = \int_0^{\infty} d\mathbf{r}_{\parallel} e^{i\mathbf{k}_{\parallel} \cdot \mathbf{r}_{\parallel}} \hat{p}(\mathbf{r}_{\parallel}, z, s)$, and the magnitude of the wave vector, \mathbf{k}_{\parallel} , i.e. $k_{\parallel} = |\mathbf{k}_{\parallel}|$,
 97 respectively.

98 The first two non-vanishing moments, $\Delta_2(t) [\equiv \langle \Delta \mathbf{r}_{\parallel}(t)^2 \rangle]$ and $\Delta_4(t) [\equiv \langle \Delta \mathbf{r}_{\parallel}(t)^4 \rangle]$, of
 99 the distribution of the lateral displacement $\Delta \mathbf{r}_{\parallel}(t) [\equiv \mathbf{r}_{\parallel}(t) - \mathbf{r}_{\parallel}(0)]$ are related to z -dependent
 100 displacement distribution, $p(\mathbf{r}_{\parallel}, z, t)$, by

$$101 \quad \Delta_n(t) = \int_0^{\ell} dz \int d\mathbf{r}_{\parallel} (r_{\parallel})^n p(\mathbf{r}_{\parallel}, z, t) = \int_0^{\ell} dz \Delta_n(z, t), \quad (\text{S2})$$

102 where $\Delta_n(z, t)$ is defined by $\Delta_n(z, t) = \int d\mathbf{r}_{\parallel} (r_{\parallel})^n p(\mathbf{r}_{\parallel}, z, t) = 2\pi \int_0^{\infty} dr_{\parallel} (r_{\parallel})^{n+1} p(\mathbf{r}_{\parallel}, z, t)$. The
 103 expression of $\Delta_n(z, t)$ can be obtained by the second and fourth derivatives of $\tilde{p}(\mathbf{k}_{\parallel}, z, t)$

104 with respect to k_{\parallel} and setting $k_{\parallel} = 0$ in the resulting equation, that is,

$$\begin{aligned}
\partial_{k_{\parallel}}^q \tilde{p}(k_{\parallel}, z, t) \Big|_{k_{\parallel}=0} &= \partial_{k_{\parallel}}^q \int d\mathbf{r}_{\parallel} e^{ik_{\parallel} r_{\parallel} \cos \theta} \tilde{p}(\mathbf{r}_{\parallel}, z, t) \Big|_{k_{\parallel}=0} \\
&= i^q \int d\mathbf{r}_{\parallel} \left[(r_{\parallel} \cos \theta)^q \tilde{p}(\mathbf{r}_{\parallel}, z, t) \right] \\
105 \qquad \qquad \qquad &= i^q \int_0^{\infty} dr_{\parallel} \int_0^{2\pi} d\theta r_{\parallel} \left[(r_{\parallel} \cos \theta)^q \tilde{p}(\mathbf{r}_{\parallel}, z, t) \right] \\
&= \begin{cases} -\Delta_2(z, t) / 2, & \text{for } q = 2 \\ 3\Delta_4(z, t) / 8, & \text{for } q = 4 \end{cases}
\end{aligned} \tag{S3}$$

106 where θ denotes the angle between the two vectors, \mathbf{k}_{\parallel} and \mathbf{r}_{\parallel} , defined by
107 $\cos \theta = \mathbf{k}_{\parallel} \cdot \mathbf{r}_{\parallel} / (k_{\parallel} r_{\parallel})$. Taking the mathematical operation, $\partial_{k_{\parallel}}^2 (\dots)_{k_{\parallel}=0}$, on both sides of eq S1
108 and using eq S3, we obtain

$$109 \qquad \qquad \qquad \hat{\Delta}_2(z, s) = 4(s - L(z))^{-1} \hat{\mathcal{D}}_{\parallel}(z, s) P_{eq}(z) / s. \tag{S4}$$

110 Equation S4 can be written as

$$111 \qquad \qquad \qquad \hat{\Delta}_2(z, s) = 4 \int_0^{\ell} dz_0 \hat{G}(z, s | z_0) \hat{\mathcal{D}}_{\parallel}(z_0, s) P_{eq}(z_0) / s. \tag{S5}$$

112 where $\hat{G}(z, s | z_0) \left[= (s - L(z))^{-1} \delta(z - z_0) \right]$ denotes the Laplace transform of Green's function
113 $G(z, t | z_0)$ defined by $\partial_t G(z, t | z_0) = L(z)G(z, t | z_0)$, with the initial condition,
114 $G(z, 0 | z_0) = \delta(z - z_0)$. The Green's function represents the conditional probability that a water
115 molecule initially located at z_0 is found at z at time t . Integrating both sides of eq S5 over z ,
116 and using the normalization condition, $\int_0^{\ell} dz G(z, t | z_0) = 1$, we obtain

$$117 \qquad \qquad \qquad \hat{\Delta}_2(s) = 4 \langle \hat{\mathcal{D}}_{\parallel}(s) \rangle / s^2. \tag{S6}$$

118 The analytic expression of $\Delta_4(t)$ can be obtained by following a similar line of

119 derivation. Taking the mathematical operation, $\partial_{k_{\parallel}}^4 (\dots)_{k_{\parallel}=0}$, on both sides of eq S1 and using
 120 eq S3, we obtain

$$121 \quad \hat{\Delta}_4(z, s) = 64 \int_0^\ell dz_1 \int_0^\ell dz_0 \hat{G}(z, s | z_1) \hat{\mathcal{D}}_{\parallel}(z_1, s) \hat{G}(z_1, s | z_0) \hat{\mathcal{D}}_{\parallel}(z_0, s) P_{eq}(z_0) / s. \quad (\text{S7})$$

122 Integrating both sides of eq S7 over z , and using the normalization condition,

$$123 \quad \int_0^\ell dz G(z, t | z_0) = 1, \text{ we obtain}$$

$$124 \quad \hat{\Delta}_4(s) = \frac{64}{s^3} \langle \hat{\mathcal{D}}_{\parallel}(s) \rangle^2 (1 + s \hat{C}_{\mathcal{D}}(s)) = 4s \hat{\Delta}_2(s)^2 (1 + s \hat{C}_{\mathcal{D}}(s)), \quad (\text{S8})$$

125 where $C_{\mathcal{D}}(t)$ denotes the lateral diffusion kernel correlation (DKC) defined by

$$126 \quad \hat{C}_{\mathcal{D}}(s) = \int_0^\ell dz \int_0^\ell dz_0 \frac{\delta \hat{\mathcal{D}}_{\parallel}(z, s)}{\langle \hat{\mathcal{D}}_{\parallel}(s) \rangle} \hat{G}(z, s | z_0) \frac{\delta \hat{\mathcal{D}}_{\parallel}(z_0, s)}{\langle \hat{\mathcal{D}}_{\parallel}(s) \rangle} P_{eq}(z_0). \quad (\text{S9})$$

127 Here, the lower and upper bounds, 0 and ℓ , of the integral denote the positions of two different
 128 membrane centers. That is to say, ℓ denotes the separation between the two lipid membrane
 129 centers (see Figure 1).

130 After the onset of Fickian diffusion, the MSD linearly increases with time because the
 131 mean diffusion kernel, $\langle \mathcal{D}_{\parallel}(z, t) \rangle$, is negligibly small at the time scale of Fickian diffusion,
 132 where we have $\Delta_2(t) = 4 \int_0^t d\tau (t - \tau) \langle \mathcal{D}_{\parallel}(\tau) \rangle \cong 4t \int_0^\infty \langle \mathcal{D}_{\parallel}(\tau) \rangle$. After the onset of Fickian
 133 diffusion, the diffusion kernel, $\hat{\mathcal{D}}_{\parallel}(z, s)$, can be replaced by its small- s limit value, $\hat{\mathcal{D}}_{\parallel}(z, 0)$,
 134 which is nothing but the lateral diffusion coefficient, $D_{\parallel}(z)$, of water molecules at longitudinal
 135 position z . Additionally, after the onset of Fickian diffusion, $L(z)$ in eq 1 can be
 136 approximated by the Smoluchowski operator, defined as, $L_{SM}(z) = \partial_z [D_{\perp}(z) (\partial_z + \partial_z \beta U(z))]$.

137 Here, $D_{\perp}(z)$ and $\beta U(z)$ respectively denote the z -dependent diffusion coefficient
 138 associated with the thermal motion of water molecules in the longitudinal direction and the
 139 thermal energy-scaled potential of mean force. Throughout β denotes $\beta = 1/k_B T$ where
 140 k_B and T denote the Boltzmann constant and temperature, respectively. Therefore, at the time
 141 scales of Fickian diffusion, the exact expression of the first two non-vanishing moments, eqs
 142 S6 and S8, can be approximated as

$$143 \quad \Delta_2(t) = 4\langle D_{\parallel} \rangle t, \quad (\text{S10})$$

$$144 \quad \Delta_4(t) = 32\langle D_{\parallel} \rangle^2 \left[t^2 + 2\eta_D^2 \int_0^t dt' (t-t') \phi_D(t') \right]. \quad (\text{S11})$$

145 Here, $\langle D_{\parallel} \rangle$ and $\eta_D^2 [= \langle \delta D_{\parallel}(z)^2 \rangle / \langle D_{\parallel} \rangle^2]$ respectively denote, the mean diffusion coefficient
 146 and the relative variance of the z -dependent lateral diffusion coefficient. $\phi_D(t)$ represents the
 147 normalized time-correlation function (TCF) of the lateral diffusion coefficient fluctuation given
 148 by

$$149 \quad \phi_D(t) = \frac{\langle \delta D_{\parallel}(t) \delta D_{\parallel}(0) \rangle}{\langle \delta D_{\parallel}^2 \rangle} = \langle \delta D_{\parallel}^2 \rangle^{-1} \int_0^{\ell} dz \int_0^{\ell} dz_0 \delta D_{\parallel}(z) G_{\text{SM}}(z, t | z_0) \delta D_{\parallel}(z_0) P_{eq}(z_0), \quad (\text{S12})$$

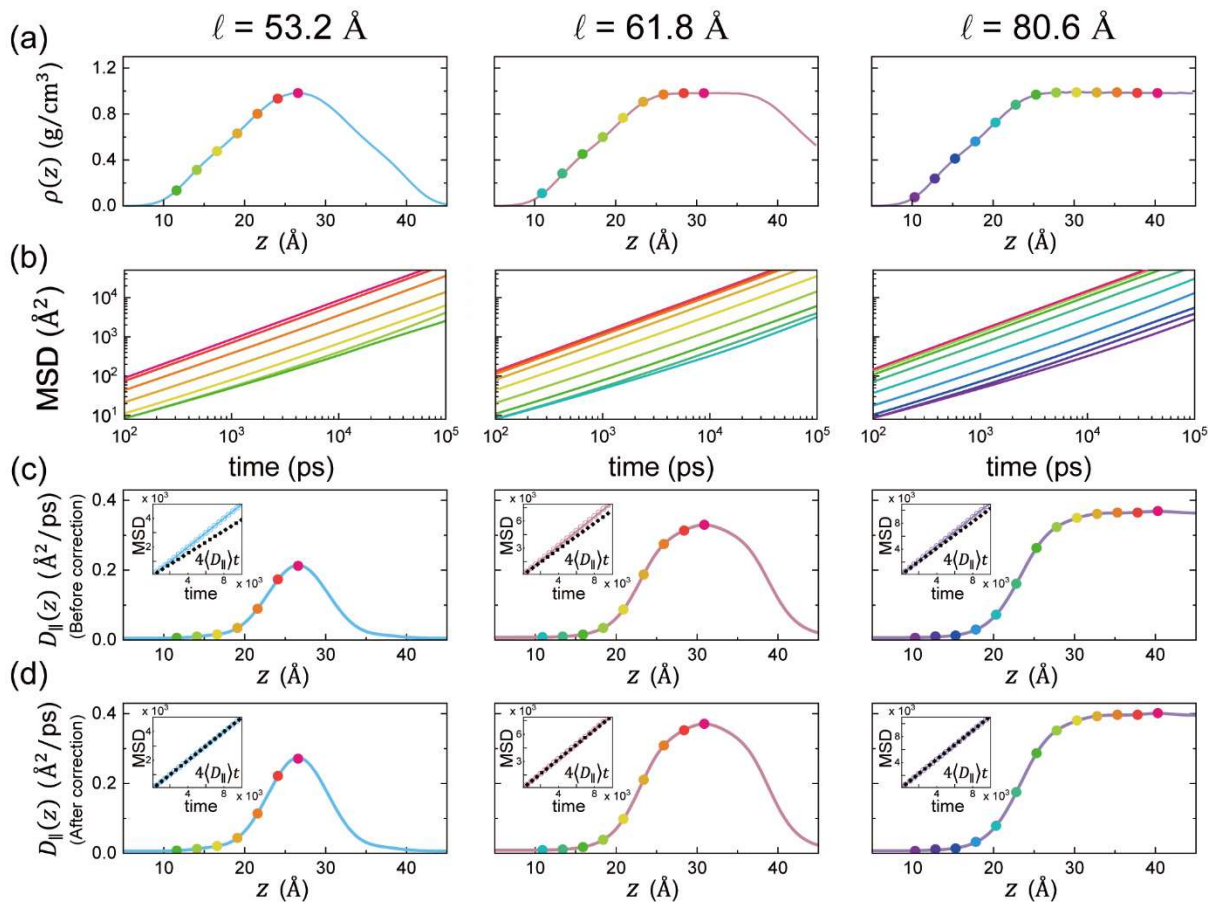
150 where $G_{\text{SM}}(z, t | z_0)$ designates Green's function defined by $\partial_t G_{\text{SM}}(z, t | z_0)$
 151 $= L_{\text{SM}}(z) G_{\text{SM}}(z, t | z_0)$, with the initial condition, $G_{\text{SM}}(z, 0 | z_0) = \delta(z - z_0)$.

152 Substituting the eqs S10 and S11 into the definition of the NGP, $\alpha_2(t)$
 153 $[\equiv \Delta_4(t)/(2\Delta_2(t)^2) - 1]$, we obtain the analytical expressions of the NGP time profile as

$$154 \quad \alpha_2(t) = \frac{2\eta_D^2}{t^2} \int_0^t dt' (t-t') \phi_D(t'). \quad (\text{S13})$$

155 Equations S6, S8, S10, and S13 are equivalent to eqs 2a, 2b, 4a, and 4b in the main text,
156 respectively.

157 Figure S1: z-dependent profiles of lateral diffusion coefficient



158

159 To determine the z-dependent profile of the lateral diffusion coefficient, we obtain the z-
 160 dependence of the MSD of water molecules in the intermembrane space. For this purpose, we
 161 estimate the MSD time profile of water molecules within each layer region defined by
 162 $z_0 - 1.5\text{\AA} \leq z \leq z_0 + 1.5\text{\AA}$, systematically changing the center position z_0 of the layer. It is
 163 difficult to estimate the long-time behavior of the MSD accurately, because very few water
 164 molecules remain in the initial layer at long times¹¹. To circumvent this difficulty, we employ
 165 a constrained MD simulation in which we randomly choose approximately 10 % of water
 166 molecules within a layer and apply Harmonic potential, $U(z) = k(z - z_0)^2$ to the chosen
 167 water molecules. Here, k represents the spring constant whose value is set to be 1.25 [Kcal/(mol

168 $\cdot \text{\AA}^2]$.

169 For the first round of our constrained simulation, we set the value of z_0 to be $\ell/2$. Then
170 we repeatedly perform the constrained simulation, systematically changing the value of z_0 by
171 2.5 \AA , until we span the entire intermembrane space. The position of z_0 for each simulation
172 is represented by a colored dot in Figure S1a. In the constrained MD simulation, the MD
173 trajectories were recorded every 10 ps during $1 \mu\text{s}$ -long NVT simulations. The number of water
174 molecules constrained by the harmonic potential is about 6% for each system, which amounts
175 to 403, 240, and 168 for the system with $\ell = 80.6 \text{ \AA}$, 61.8 \AA , and 53.2 \AA .

176 From the trajectories of water molecules constrained by the harmonic potential, we
177 obtained the MSDs of the lateral water displacement for every layer of the simulation system
178 with different intermembrane separations (Figure S1b). Each solid line in Figure S1b represents
179 the MSD obtained from the constrained MD simulation with z_0 at the position marked by the
180 dot of the same color in Figure S1a. From the long-time MSD profile, we estimate the lateral
181 diffusion coefficient at each z position by $D_{\parallel}(z) = \lim_{t \rightarrow \infty} \Delta_2(z, t)/4t$. These values are shown
182 as circle symbols in Figure S1c. The resulting profile of the lateral diffusion coefficient can
183 well be fitted to the multi-Gaussian function,

$$184 \quad D_{\parallel}(z) = y_0 + \sum_{i=1}^n \frac{a_i}{\omega_i \sqrt{\pi/2}} \exp\left(-2 \left(\frac{z - z_{c,i}}{\omega_i}\right)^2\right), \quad (\text{S14})$$

185 as shown as solid lines in Figure S1c. The optimized parameters for these fittings are provided
186 in Table S1. Using the multi-Gaussian representation of $D_{\parallel}(z)$, we calculate the mean lateral
187 diffusion coefficient, $\langle D_{\parallel} \rangle$, by

188
$$\langle D_{\parallel} \rangle = \int_0^{\ell} dz D_{\parallel}(z) P_{eq}(z) \quad (S15)$$

189 with $P_{eq}(z) = \rho(z) / \int_0^{\ell} dz \rho(z)$. Here, $\rho(z)$ denotes the mass density profile of water
 190 molecules, shown in Figure S1a.

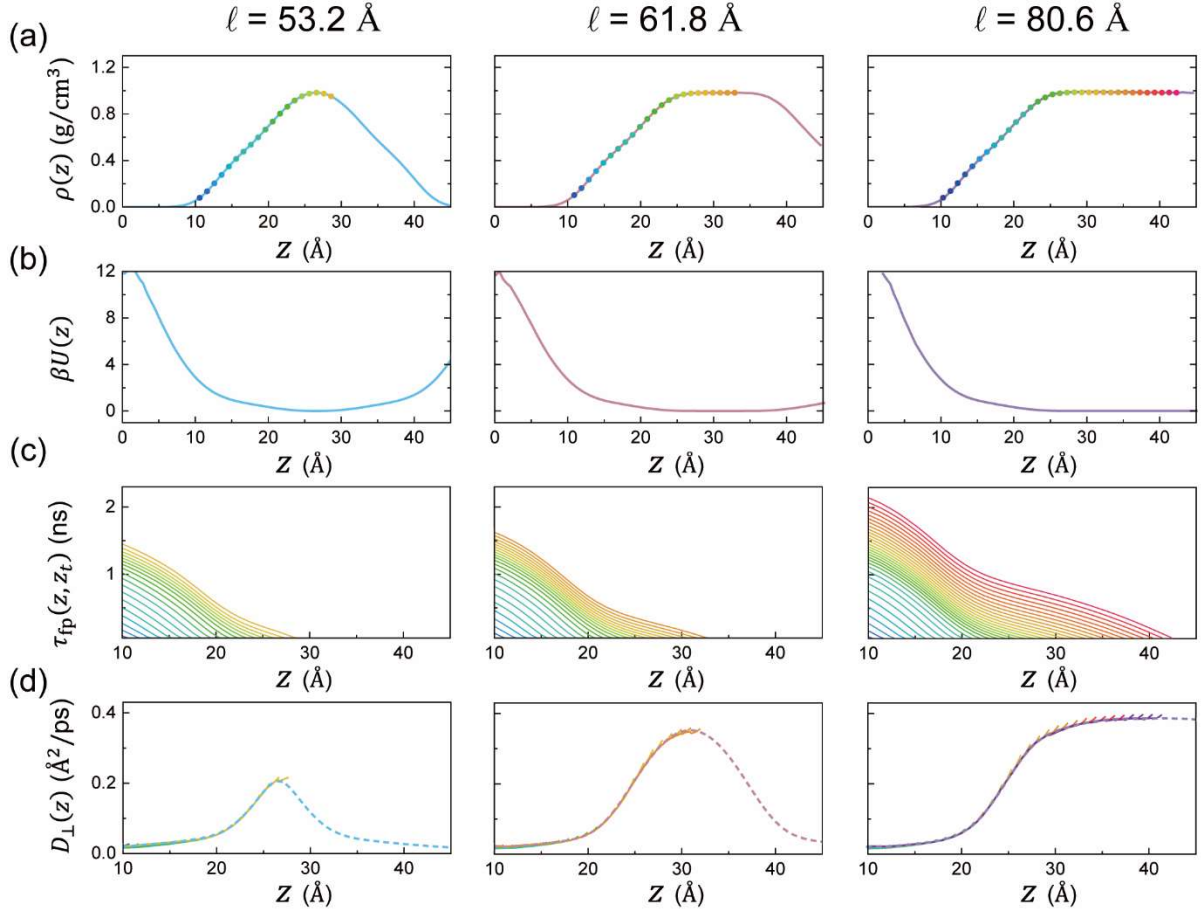
191 To test the accuracy of $D_{\parallel}(z)$ obtained from our constrained MD simulations, we
 192 compared $4\langle D_{\parallel} \rangle t$ with the MSD obtained from the simulation of the entire system as shown
 193 in insets of Figure S1c. These results clearly show that the estimation of $D_{\parallel}(z)$ and $\langle D_{\parallel} \rangle$
 194 from our constrained MD simulation is not perfectly accurate. $\langle D_{\parallel} \rangle$ estimated from our
 195 constrained MD simulation is slightly smaller than the true value of $\langle D_{\parallel} \rangle$ estimated from the
 196 MSD of the entire system. This discrepancy is expected because 10% of the water molecules
 197 are constrained in each layer by the fictitious harmonic potential, and their transport dynamics
 198 would not be exactly the same as the transport dynamics of the free water molecules moving
 199 across various layers.

200 We resolve this issue by introducing a correction factor, c , to $D_{\parallel}(z)$ estimated from our
 201 constrained MD simulation in such a way that the mean lateral diffusion coefficient calculated
 202 by $c \int_0^{\ell} dz D_{\parallel}(z) P_{eq}(z)$ is the same as the true value of $\langle D_{\parallel} \rangle$ estimated from the MSD of the
 203 entire system (see insets of Figure S1d). The values of the correction factor are 1.087, 1.124,
 204 and 1.276 for the systems with $\ell = 80.6 \text{ \AA}$, 61.8 \AA , and 53.2 \AA , respectively. The value of the
 205 corrected lateral diffusion coefficient, $cD_{\parallel}(z)$, are represented by solid lines in Figure S1d and
 206 Figure 3c in the main text.

207 We use the corrected lateral diffusion coefficient profiles in calculating the theoretical
 208 results depicted in Figure 4 of the main text. The agreement between our theoretical results and

209 the MD simulation results for the time profiles of the NGP, the TCF of the lateral diffusion
210 coefficient, and the lateral displacement distribution at various times confirms the accuracy of
211 our corrected lateral diffusion coefficient profiles.

212 Figure S2: z-dependent profiles of longitudinal diffusion coefficient



213

214

215

216

217

218

219

We obtain the longitudinal diffusion coefficient profile, $D_{\perp}(z)$, from the mean-first passage time profile (MFPT), using the method developed in Ref.^{9–11}. The MFPT, $\tau_{\text{fp}}(z, z_t)$, denotes the average time required for a water molecule initially located at z to arrive at a target position z_t . This method is based on the analytic results of the previous theories that represent $\tau_{\text{fp}}(z, z_t)$ as a functional of $D_{\perp}(z)$ and the potential of mean force, $\beta U(z)$ ^{12,13}. According to Ref. 9, $D_{\perp}(z)$ can be obtained from

220

$$D_{\perp}(z) = -\frac{e^{\beta U(z)}}{\partial \tau_{\text{fp}}(z, z_t) / \partial z} \int_{z_{\text{ref}}}^z dz' e^{-\beta U(z')}. \quad (\text{S16})$$

221

Here, thermal energy scaled potential of mean force, $\beta U(z)$, of water molecules can be

222 calculated from the density profile of water molecules, shown in Figure S2a, i.e., $\beta U(z) \equiv$
 223 $-\log[\rho(z)/\rho_{bulk}^{45^\circ C}]$ with $\rho_{bulk}^{45^\circ C}$ being the density of bulk water at 45°C. In eq S16, z_{ref}
 224 designates the position of the reflecting boundary. As the number of water molecules passing
 225 through the lipid bilayer membrane is negligibly small throughout our MD simulation, we set
 226 the reflecting boundary at the membrane center, i.e., $z_{\text{ref}} = 0$.

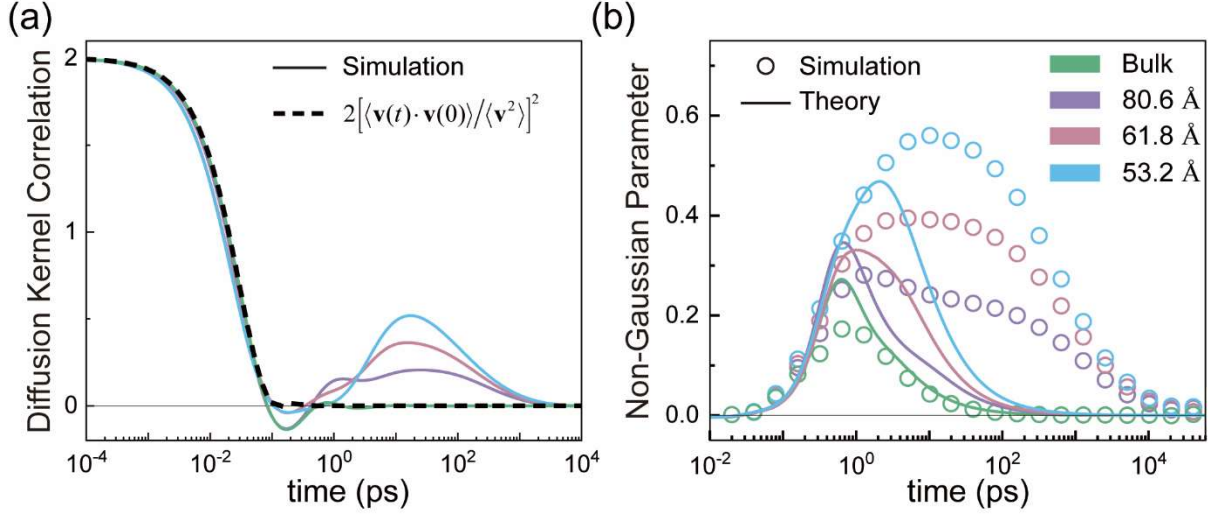
227 To calculate $D_{\perp}(z)$ using eq S16, we computed the z -dependent profile of $\tau_{\text{fp}}(z, z_t)$
 228 using our MD trajectories, systematically changing the value of z_t by 1 Å. The various
 229 positions of z_t for each system are represented by the dots of different colors in Figure S2a.
 230 The z -dependent profiles of MFPT for various values of z_t have the same slope through the
 231 entire z range, as shown in Figure S2c. Each solid line in Figure S2c represents $\tau_{\text{fp}}(z, z_t)$ with
 232 the target position, z_t , represented by the dot of the same color in Figure S2a. As $\partial_z \tau_{\text{fp}}(z, z_t)$
 233 is independent of z_t , so is $D_{\perp}(z)$ calculated from eq S15 (see Figure S2d). The profile of
 234 $D_{\perp}(z)$ was well fitted to a multi-Gaussian function,

$$235 \quad D_{\perp}(z) = y_0 + \sum_{i=1}^n \frac{a_i}{\omega_i \sqrt{\pi/2}} \exp\left[-2\left(\frac{z - z_{c,i}}{\omega_i}\right)^2\right], \quad (\text{S17})$$

236 shown as dotted lines in Figure S2d. The optimized parameters for these fittings are provided
 237 in Table S2. These best-fitted results, shown as dotted lines in Figure S2d, are represented by
 238 the solid lines in Figure 3d of the main text.

239

240 Figure S3: Diffusion Kernel Correlation and Non-Gaussian Parameter



241

242 The lateral diffusion kernel correlation (DKC), $C_D(t)$, is a key dynamic quantity that
 243 characterizes the environment-coupled fluctuation of water molecule's motility in the lateral
 244 direction. Based on the eq S8, we express the DKC in the Laplace domain as

$$245 \quad \hat{C}_D(s) = \frac{\hat{\Delta}_4(s)}{4s^2 \hat{\Delta}_2(s)^2} - \frac{1}{s} \quad (\text{S18})$$

246 To extract the time-profile of the DKC of water molecules by performing numerical inverse
 247 Laplace transform of eq S18, it is convenient to have analytic expressions of the first two non-
 248 vanishing moments, $\Delta_2(t)$ and $\Delta_4(t)$, of the distribution of the lateral displacement of water
 249 molecules.

250 The time profile of the MSD, $\Delta_2(t)$, is well represented by the following formula
 251 according to Ref.14:

$$252 \quad \Delta_2(t) = 4 \frac{k_B T}{M \gamma_0^2} c_0 (\gamma_0 t - 1 + e^{-\gamma_0 t}) + 4 \frac{k_B T}{M} \sum_{i=1}^2 \frac{c_i}{\omega_{0,i}^2} \left[1 - e^{-\gamma_i t} \left(\cosh \omega_i t + \frac{\gamma_i}{\omega_i} \sinh \omega_i t \right) \right] \quad (\text{S19})$$

253 This formula represents the MSD of a bead in a Gaussian polymer composed of three beads in

254 a high friction regime. The first and second terms on the R.H.S of eq 19 account for the
 255 contribution from the unbound mode and bound modes, respectively. c_i designates the weight
 256 coefficient of i th mode, which satisfies the following condition $\sum_{j=0}^2 c_j = 1$. The optimized
 257 parameters for this fitting are provided in Table S3.

258 The analytic expression of the fourth moment, $\Delta_4(t)$, is obtained from

$$259 \quad \Delta_4(t) = 2\Delta_2(t)^2[1 + \alpha_2(t)] \quad (\text{S20})$$

260 which is obtained from the definition of the NGP. The simulation result for the time profile of
 261 the NGP, or $\alpha_2(t)$, could be well fitted to the following function (see Figure 2):

$$262 \quad \alpha_2(t) \cong \sum_{i=1}^{2\text{or}3} a_i \exp\left[-(\log_{10} t - b_i)^2 / c_i\right]. \quad (\text{S21})$$

263 The optimized parameters for this fitting are provided in Table S4. Substituting eqs S19 and
 264 S21 into eq S20, we obtain the fully analytic expression of the fourth moment.

265 Taking the Laplace transforms of $\Delta_2(t)$ and $\Delta_4(t)$, and substituting the results into eq
 266 S18, we obtain the expression of DKC in the Laplace domain. To obtain the value of DKC at a
 267 specific timepoint, t , we perform the numerical Laplace inversion of eq S18, by using the
 268 Stehfest algorithm. These results are shown in Figure S3 and Figure 4a. The DKC values in
 269 various conditions are shown as solid lines in Figure S3a. At short times, where MSD is not
 270 linear in time yet, the DKC can be approximated by $C_D^{(short)}(t) = 2[\langle \mathbf{v}(t) \cdot \mathbf{v}(0) \rangle / \langle \mathbf{v}^2 \rangle]^2 = 2\phi_v^2(t)$
 271 ¹⁴. Here, \mathbf{v} denotes the water molecule's velocity vector in the lateral direction, and the
 272 velocity autocorrelation function, $\langle \mathbf{v}(t) \cdot \mathbf{v}(0) \rangle$, is equivalent to twice the lateral diffusion
 273 kernel, $\langle \mathcal{D}_{\parallel}(t) \rangle$ ¹⁴. From eqs S6 and S19, an analytic expression of the lateral diffusion kernel

274 can be obtained as

$$275 \quad \frac{\langle \mathcal{D}_{\parallel}(t) \rangle}{\langle \mathcal{D}_{\parallel}(0) \rangle} \left(= \frac{\langle \mathbf{v}(t) \cdot \mathbf{v}(0) \rangle}{\langle |\mathbf{v}|^2 \rangle} \right) = c_0 e^{-\gamma_0 t} + \sum_{i=1}^2 c_i e^{-\gamma_i t} \left[\cosh \omega_i t + \frac{\gamma_i}{\omega_i} \sinh \omega_i t \right] \quad (\text{S22})$$

276 where $\langle \mathcal{D}_{\parallel}(0) \rangle$ denotes $k_B T / M$.

277 To verify the correctness of $C_D(t) \cong 2\phi_v^2(t)$, we made a comparison between $2\phi_v^2(t)$ of
 278 bulk water, depicted as the dashed line in Figure S3, and the time profile of the DKCs. The
 279 agreement between $2\phi_v^2(t)$ and the DKCs at short times confirms the validity of our short-
 280 time asymptotic expression of the DKC. As shown in Figure S3a, the short-time dynamics of
 281 the DKC is largely independent of the degree of confinement, or ℓ .

282 The short-time asymptotic expression of the DKC enables us to obtain the short-time
 283 asymptotic behavior of $\alpha_2(t) \propto t^2$. Using the asymptotic expression of the DKC in the exact
 284 analytic expression of the fourth moment, given in eq S8, we obtain

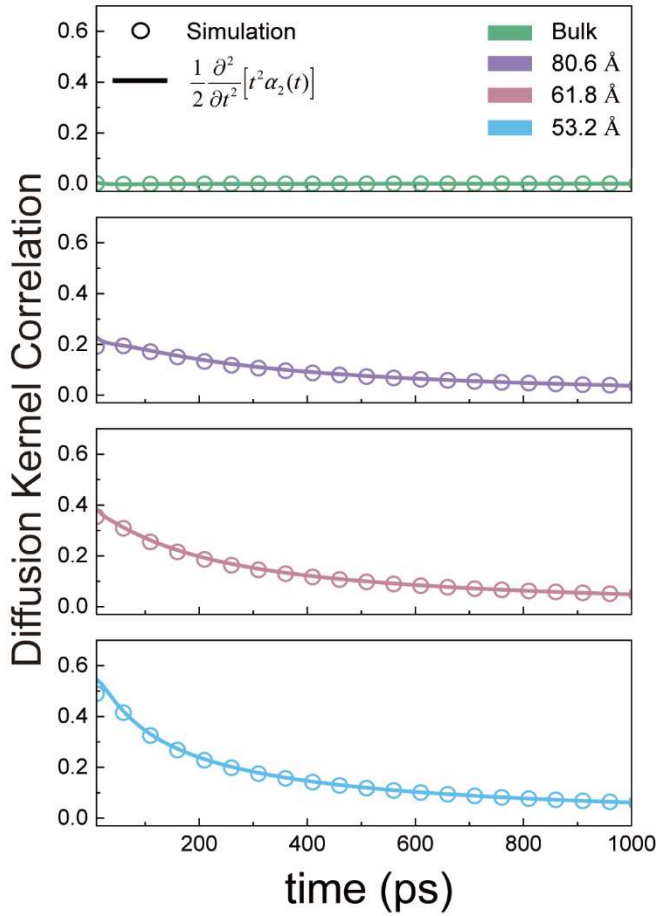
$$285 \quad \hat{\Delta}_4(s) \cong 4s \hat{\Delta}_2(s)^2 [1 + s \hat{C}_D^{(short)}(s)]. \quad (\text{S23})$$

286 Substituting the time-domain version of eq S23 into the definition of the NGP, $\alpha_2(t)$
 287 $[\equiv \Delta_4(t)/(2\Delta_2(t)^2) - 1]$, we obtain the following short-time asymptotic expression of $\alpha_2(t)$:

$$288 \quad \alpha_2(t) = \frac{1}{18} (\gamma^2 - \mu) t^2 + \mathcal{O}(t^3) \quad (\text{S24})$$

289 In eq S24, γ and μ are given by $\gamma = -\lim_{t \rightarrow 0} \partial \phi_v(t) / \partial t = c_0 \gamma_0 + 2 \sum_{i=1}^n c_i \gamma_i$ and
 290 $\mu = \lim_{t \rightarrow 0} \partial^2 \phi_v(t) / \partial t^2 = c_0 \gamma_0^2 + \sum_{i=1}^n c_i (3\gamma_i^2 + \omega_i^2)$, respectively¹⁴. These results are shown as
 291 the solid lines in Figure S3b. The short-time asymptotic behavior of the NGP given in eq S24
 292 is found to be in good quantitative agreement with our MD simulations results.

293 Figure S4: Relationship between DKC and NGP at long times



294

295 The relaxation dynamics of the DKC, $C_D(t)$, determines the NGP time profile of water
 296 molecules in the intermembrane space after the onset of Fickian diffusion, where the time
 297 profile of $C_D(t)$ can be obtained by the NGP time profile, i.e.,

298
$$C_D(t) \cong \eta_D^2 \phi_D(t) = \frac{1}{2} \frac{\partial^2}{\partial t^2} [t^2 \alpha_2(t)]. \quad (\text{S25})$$

299 Solid lines in Figure S4 represent the time profiles of $C_D(t)$ obtained from eqs S25 and S21.

300 Circles represent the time profiles of $C_D(t)$ extracted from our MD simulation results, using
 301 the method described in the paragraph below Figure S3.

302

303 Movie S1: Heatmap of discrete Green's function

304 As we mentioned in the main text, linear dependence between τ_D and ℓ^2 , as shown in
305 the inset of Figure 4a, arises because the time taken for water molecules to traverse the entire
306 intermembrane space increases quadratically with separation, ℓ , between center membranes.
307 To show the stochastic transport dynamics of water molecules at various initial positions, we
308 present a movie showing the time-dependent changes in the probability distribution of water
309 molecules in the intermembrane space. For this purpose, we first discretize the intermembrane
310 space into three regions: two interfacial regions near the two membranes confining the water
311 molecules, defined by $z < z_c$ and $z > \ell - z_c$ with $z_c = 23.6 \text{ \AA}$, and one bulk water-like
312 region between the two interfacial regions (see Figure 3 in the main text). The bulk water-like
313 region does not exist for our system with $\ell = 53.2 \text{ \AA}$; however, it exists for our system with
314 a greater value of intermembrane separation ℓ .

315 We identify the entire bulk water-like region as a single layer named layer 0. Each
316 interfacial water region is divided into 5 layers. Specifically, the interfacial water region on the
317 left side is divided into the following layers: (i) $0 \text{ \AA} \leq z < 15.2 \text{ \AA}$, (ii) $15.2 \leq z < 18 \text{ \AA}$, (iii)
318 $18 \text{ \AA} \leq z < 20.8 \text{ \AA}$, (iv) $20.8 \text{ \AA} \leq z < 23.6 \text{ \AA}$, and (v) $23.6 \text{ \AA} \leq z < z_c (= 26.6 \text{ \AA})$. These
319 layers are respectively labeled as -5, -4, -3, -2, and -1 layers. Similarly, the interfacial water
320 region on the right side is divided from the membrane center on the right side with identical
321 widths, and the corresponding layers are designated as 5, 4, 3, 2, 1 layer, respectively.
322 Consequently, the total number of layers is 11 for $\ell = 80.6 \text{ \AA}$ and $\ell = 61.8 \text{ \AA}$, and 10 for
323 $\ell = 53.2 \text{ \AA}$.

324 In Supplemental Movie, we show how the spatial distribution of water molecules in each
325 layer changes over time. For this purpose, we present heat maps, each of which represents the
326 probability distribution of water molecules for our system at a given time. In each heat map,
327 the color of the cell in the n -th column and m -th row represents the probability, $g(n, t|m)$, that
328 a water molecule initially located in the m -th layer is found in the n -th layer at time t . By
329 definition, the initial condition of $g(n, t|m)$ is given by $\lim_{t \rightarrow 0} g(n, t|m) = \delta_{nm}$ where δ_{nm}
330 designates Kronecker's delta.

331 The evolving heatmap patterns, as shown in Supplemental Movie, clearly demonstrate
332 that the time required to reach the equilibrium state increases with the length of ℓ . Specifically,
333 in the system with $\ell = 80.6 \text{ \AA}$, water molecules located in the interfacial region do not
334 transfer to the opposite side of the interfacial water region within the first 50 ps. This behavior
335 can be attributed to the increased size of the bulk-water-like region, which hinders the fast
336 exchange of water molecules between the interfacial water regions.

337 Supplemental Tables

ℓ (Å)	80.6	61.8	53.2
y_0	0.007	0.008	0.005
a_1	0.636	0.374	0.029
a_2	0.636	0.374	0.029
a_3	5.061	4.412	1.951
a_4	5.061		
a_5	0.721		
ω_1	5.944	4.797	4.079
ω_2	5.944	4.797	4.079
ω_3	12.226	11.100	7.449
ω_4	12.226		
ω_5	7.060		
$z_{c,1}$	-14.750	-6.131	-10.790
$z_{c,2}$	14.750	6.131	10.790
$z_{c,3}$	-8.002	0	0
$z_{c,4}$	8.002		
$z_{c,5}$	0		

338 **Table S1.** Lateral diffusion coefficient fitting parameters (eq S14).

339

ℓ (Å)	80.6	61.8	53.2
y_0	0.021	0.018	0.014
a_1	0.063	-0.400	0.973
a_2	0.058	-0.400	0.953
a_3	3.122	5.460	0.055
a_4	2.286		
a_5	1.015		
a_6	0.974		
a_7	2.138		
a_8	1.826		
ω_1	5.873	6.282	5.554
ω_2	5.856	6.281	16.780
ω_3	8.568	12.991	1.901
ω_4	8.089		
ω_5	5.958		
ω_6	6.136		
ω_7	7.413		
ω_8	13.114		
$z_{c,1}$	-22.820	-9.125	0
$z_{c,2}$	22.777	9.125	0
$z_{c,3}$	-11.448	0	0
$z_{c,4}$	11.914		
$z_{c,5}$	-5.603		
$z_{c,6}$	5.456		
$z_{c,7}$	-0.453		
$z_{c,8}$	5.456		

340

Table S2. Longitudinal diffusion coefficient fitting parameters (eq S17).

341

	Bulk	$\ell = 80.6 \text{ \AA}$	$\ell = 61.8 \text{ \AA}$	$\ell = 53.2 \text{ \AA}$
c_0	0.0552	0.0624	0.0126	0.0970
c_1	0.0386	0.0403	0.4937	0.4515
c_2	0.9062	0.8973	0.4937	0.4515
γ_0	2.0867	3.2698	0.9116	11.4206
γ_1	2.1041	4.9715	9.8813	11.4206
γ_2	9.1332	9.5602	11.0886	11.7578
$\omega_{0,1}$	2.1041	1.8450	9.8813	11.4206
$\omega_{0,2}$	9.1332	9.5602	4.4480	6.0659
ω_1	0.0017	4.6165	0.0001	0.0002
ω_2	0.0018	0.0026	10.1574	6.0659

342 **Table S3.** Diffusion Kernel fitting parameters (eq S19).

343

344

345

346

	Bulk	$\ell = 80.6 \text{ \AA}$	$\ell = 61.8 \text{ \AA}$	$\ell = 53.2 \text{ \AA}$
a_1	0.166	0.247	0.269	0.263
a_2	0.021	0.105	0.131	0.513
a_3		0.191	0.330	
b_1	-0.111	0.007	0.018	0.210
b_2	0.961	1.041	0.916	1.633
b_3		2.148	1.925	
c_1	0.606	0.637	0.618	0.817
c_2	0.713	0.584	0.607	2.279
c_3		1.634	1.864	

347 **Table S4.** NGP fitting parameters (eq S21).

348

349 Reference

- 350 (1) Lee, J.; Cheng, X.; Swails, J. M.; Yeom, M. S.; Eastman, P. K.; Lemkul, J. A.; Wei, S.;
351 Buckner, J.; Jeong, J. C.; Qi, Y.; Jo, S.; Pande, V. S.; Case, D. A.; Brooks, C. L.;
352 MacKerell, A. D.; Klauda, J. B.; Im, W. CHARMM-GUI Input Generator for NAMD,
353 GROMACS, AMBER, OpenMM, and CHARMM/OpenMM Simulations Using the
354 CHARMM36 Additive Force Field. *J Chem Theory Comput* **2016**, *12* (1), 405–413.
355 <https://doi.org/10.1021/acs.jctc.5b00935>.
- 356 (2) Lee, J.; Hitzenberger, M.; Rieger, M.; Kern, N. R.; Zacharias, M.; Im, W. CHARMM-
357 GUI Supports the Amber Force Fields. *J Chem Phys* **2020**, *153* (3), 035103.
358 <https://doi.org/10.1063/5.0012280>.
- 359 (3) Wu, E. L.; Cheng, X.; Jo, S.; Rui, H.; Song, K. C.; Dávila-Contreras, E. M.; Qi, Y.; Lee,
360 J.; Monje-Galvan, V.; Venable, R. M.; Klauda, J. B.; Im, W. CHARMM-GUI *Membrane*
361 *Builder* toward Realistic Biological Membrane Simulations. *J Comput Chem* **2014**, *35*
362 (27), 1997–2004. <https://doi.org/10.1002/jcc.23702>.
- 363 (4) Jo, S.; Lim, J. B.; Klauda, J. B.; Im, W. CHARMM-GUI Membrane Builder for Mixed
364 Bilayers and Its Application to Yeast Membranes. *Biophys J* **2009**, *97* (1), 50–58.
365 <https://doi.org/10.1016/j.bpj.2009.04.013>.
- 366 (5) Jo, S.; Kim, T.; Im, W. Automated Builder and Database of Protein/Membrane
367 Complexes for Molecular Dynamics Simulations. *PLoS One* **2007**, *2* (9), e880.
368 <https://doi.org/10.1371/journal.pone.0000880>.
- 369 (6) Jo, S.; Kim, T.; Iyer, V. G.; Im, W. CHARMM-GUI: A Web-based Graphical User
370 Interface for CHARMM. *J Comput Chem* **2008**, *29* (11), 1859–1865.
371 <https://doi.org/10.1002/jcc.20945>.

- 372 (7) Dickson, C. J.; Madej, B. D.; Skjevik, Å. A.; Betz, R. M.; Teigen, K.; Gould, I. R.;
373 Walker, R. C. Lipid14: The Amber Lipid Force Field. *J Chem Theory Comput* **2014**, *10*
374 (2), 865–879. <https://doi.org/10.1021/ct4010307>.
- 375 (8) Darden, T.; York, D.; Pedersen, L. Particle Mesh Ewald: An $N \cdot \log(N)$ Method for Ewald
376 Sums in Large Systems. *J Chem Phys* **1993**, *98* (12), 10089–10092.
377 <https://doi.org/10.1063/1.464397>.
- 378 (9) Hinczewski, M.; Von Hansen, Y.; Dzubiella, J.; Netz, R. R. How the Diffusivity Profile
379 Reduces the Arbitrariness of Protein Folding Free Energies. *Journal of Chemical*
380 *Physics* **2010**, *132* (24). <https://doi.org/10.1063/1.3442716>.
- 381 (10) Sedlmeier, F.; von Hansen, Y.; Mengyu, L.; Horinek, D.; Netz, R. R. Water Dynamics at
382 Interfaces and Solutes: Disentangling Free Energy and Diffusivity Contributions. *J Stat*
383 *Phys* **2011**, *145* (2), 240–252. <https://doi.org/10.1007/s10955-011-0338-0>.
- 384 (11) von Hansen, Y.; Gekle, S.; Netz, R. R. Anomalous Anisotropic Diffusion Dynamics of
385 Hydration Water at Lipid Membranes. *Phys Rev Lett* **2013**, *111* (11), 118103.
386 <https://doi.org/10.1103/PhysRevLett.111.118103>.
- 387 (12) Weiss, G. H. First Passage Time Problems in Chemical Physics; 1967; pp 1–18.
388 <https://doi.org/10.1002/9780470140154.ch1>.
- 389 (13) Szabo, A.; Schulten, K.; Schulten, Z. First Passage Time Approach to Diffusion
390 Controlled Reactions. *J Chem Phys* **1980**, *72* (8), 4350–4357.
391 <https://doi.org/10.1063/1.439715>.
- 392 (14) Song, S.; Park, S. J.; Kim, M.; Kim, J. S.; Sung, B. J.; Lee, S.; Kim, J.-H.; Sung, J.
393 Transport Dynamics of Complex Fluids. *Proceedings of the National Academy of*
394 *Sciences* **2019**, *116* (26), 12733–12742. <https://doi.org/10.1073/pnas.1900239116>.

395

396